Comparison of beamforming and spectral autocorrelation method applied on ambient noise data acquired with a small aperture array

Soumen Koley[1*], Xander Campman[2], Mark Beker[3], Jo van den Brand[1], Maria Bader[1] and Henk Jan Bulten[1] report on the benefits and the constraints on beamforming and spectral autocorrelation on ambient noise data acquired with a small aperture array deployed at Groningen, the Netherlands.

Introduction

Passive seismic methods use the seismic noise produced by natural and anthropogenic sources to image the subsurface. Seismic waves generated by ocean waves hitting against a shore or those generated by earthquakes are some examples of naturally occurring seismic noise sources. Artificial sources of seismic noise are due to human activities. Cars driving on a road, ground vibrations created by farming activities or vibrations induced into the ground by bridges are examples of anthropogenic seismic excitation. Seismic waves generated from these sources propagate through the Earth's surface both as body and surface waves. In passive seismic studies, we measure the ground motion mainly due to surface waves propagating along the surface of the Earth and use it to infer information about shallow subsurface geological structures. The dominant contribution of surface waves to the seismic wavefield can be due to both the source mechanism (Draganov et al., 2009) and the stationary phase arguments about the noise source (Kimman and Trampert, 2010). Since the surface waves propagating along the surface of the Earth can be treated as plane waves in the far field, array techniques for computing the velocity and azimuth of propagation of these surface waves are well suited (Park et al., 1999).

The frequency-wavenumber method (f-k) and the Extended Spectral Auto-Correlation (ESAC) method are two data processing techniques used to obtain the surface wave phase velocities from ambient seismic noise measurements. The f-k method is also sometimes referred to as beamforming (Lacoss et al. in 1969). Beamforming has been widely used in studies by various researchers, for example, Asten and Henstridge (1984), Horike (1985), Okada et al. (1987). On the contrary, the ESAC method, which can estimate surface wave phase velocities more accurately than beamforming (Ohori et al., 2002), was seldom used by geophysicists due to restrictions on the sensor layout and because most of the work has been reported in Japanese. It was not until the work of Ohori et al. (2002) who reported the work previously done by Okada et al. (1987) and Chouet et al. (1998) that the method gained popularity. The ESAC method is an extension to the SAC method originally proposed by Aki (1957). However, due to the limitation that the SAC method could only be used for circular arrays, it has been used only by a few researchers. Ohori et al. (2002) extended the SAC method such that it could be used for arbitrary array geometry and named it ESAC. The ESAC method assumes that over a long recording time of seismic noise, the sources of noise illuminate the array isotropically. The ESAC method does not provide any information about the direction of propagation of the surface waves, unlike the f-k method which is slightly advantageous in this regard. In the next sections of this article we discuss the two passive seismic data analysis methods and compare their performance based on seismic noise data acquired at Wittewierum, Groningen in the north of the Netherlands.

Array properties

Ambient seismic noise was recorded by an array of 96 vertical component 5 Hz wireless Tremornet nodes in Groningen for a period of three weeks between 5-22 January, 2016 (Beker etal. 2017). This passive seismic study was conducted in collaboration with Shell and Innoseis. The array recorded the vertical component of ground velocity continuously for a period of three weeks and hence was suitable for carrying out passive seismic data analysis. Figure 1a shows the array layout on a cartesian plane. Seismic sensors were deployed on a regular grid with a spacing of 100 m. The maximum inter-sensor distance was about 1200 m and the minimum was 100 m. Figure 1b shows the distribution of the inter-sensor distance and the one-way azimuth for all sensor pairs. A well spread distribution of inter-sensor distances is observed for all azimuths up to a maximum distance of 800 m. Sensor pair counts in excess of 200 are observed for the inter-sensor distance interval of 100 to 800 m, and the pair count gradually tapers off to values of less than 50 for greater inter-sensor distances (Figure. 1c). Now that the array geometry is known, it is important to identify the highest frequency of the seismic wavefield that can be sampled by the array without spatial aliasing. For this we compute the theoretical array response as proposed by Woods

[1] National Institute of Subatomic Physics | [2] Shell Global Solutions International | [3] Innoseis
[*] Corresponding author, E-mail: skoley@nikhef.nl
DOI: xxx

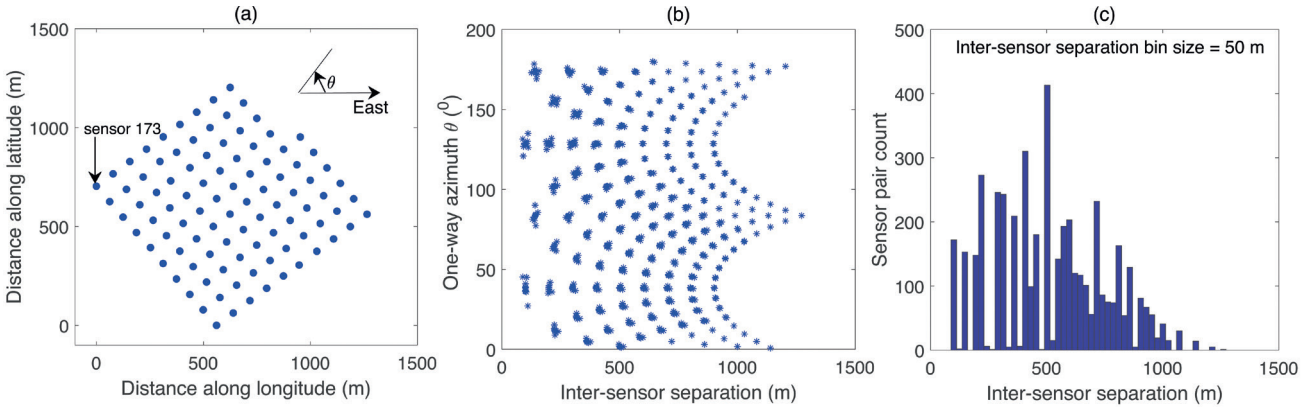

Figure 1 a) Seismic array layout at Witteweirum, Groningen shown in cartesian coordinates. The one-way azimuth (θ) is measured anticlockwise from the east. b) Distribution of one-way azimuths and inter-sensor separation corresponding to all sensor pairs. c) Histogram of the number of sensor pairs corresponding to all inter-sensor separations.

and Lintz (1973) for several sets of plane wave velocities and as well as directions of propagation corresponding to different frequencies. The surface wave phase velocities used for computing the theoretical array response are obtained from previous surface wave studies in the region (Kimman et al., 2012). A similar implementation of computing the theoretical array response has been previously discussed in Koley et al. (2017).

Figure 2 shows the computed theoretical array response values on a polar graph with slowness ~~u~~ increasing radially outwards and azimuth θ measured clockwise from the North (y-axis). Consequently, the x and the y-axis are labelled as u cos θ and u sin θ respectively. Key observations from the theoretical array response plots in Figure 2 are: lack of resolution at 0.4 Hz in determining the ray parameters of the incoming plane wave, and spatial aliasing at a frequency of 1.7 Hz. The lack of resolution of the peak in the u - θ domain corresponding to the plane wave of frequency 0.4 Hz is due to insufficient array aperture (maximum of 1200 m) as compared to the wavelength of the plane wave at 0.4 Hz which is about 3000 m. The smallest sensor separation in the array is 100 m, hence it can only sample plane waves with wavelengths of 300 m or more. As a result for our test case of a plane wave of frequency 1.7 Hz and propagating at a speed of 330 m/s and wavelength of about 194 m, we observe spatial aliasing. Figure 2c shows the two incorrect peaks observed due to spatial aliasing in the u - θ graph alongside the true peak which is observed at an azimuth of 45° and a slowness of 0.003 s/m. Thus we can conclude that with this particular array configuration, we can only estimate the speed of the Rayleigh wave propagation up to a maximum frequency of 1.7 Hz.

Ambient noise characteristics

Before proceeding with the array analysis of the seismic noise data we briefly discuss the attributes of the ambient seismic noise observed in the region. Figure 3a shows a spectrogram of the seismic ground velocity recorded between 5-22 January, 2016 by sensor 173, the location of which is shown by an arrow in Figure 1a. The temporal resolution of the spectrogram is one hour and the PSD for each hour of data is computed with a window length of ~~minutes~~ and an overlap of 50% between successive windows. Since the resonance frequency of the sensors is 5 Hz, the sensors are sensitive only down to frequencies of 0.2 Hz, below which the noise of the electronics dominate the spectrum. In the frequency band 0.2 to 0.7 Hz, a peak in the PSD is observed, which corresponds to the secondary microseism due to oceanic disturbances in the North Sea. The magnitude of the peak varies within an order of magnitude during the 18 days of measurement, with maximum microseismic noise being registered on 8 January, 2016 (Figure 3b). The magnitude of the microseism in the band 0.2 to 0.5 Hz is

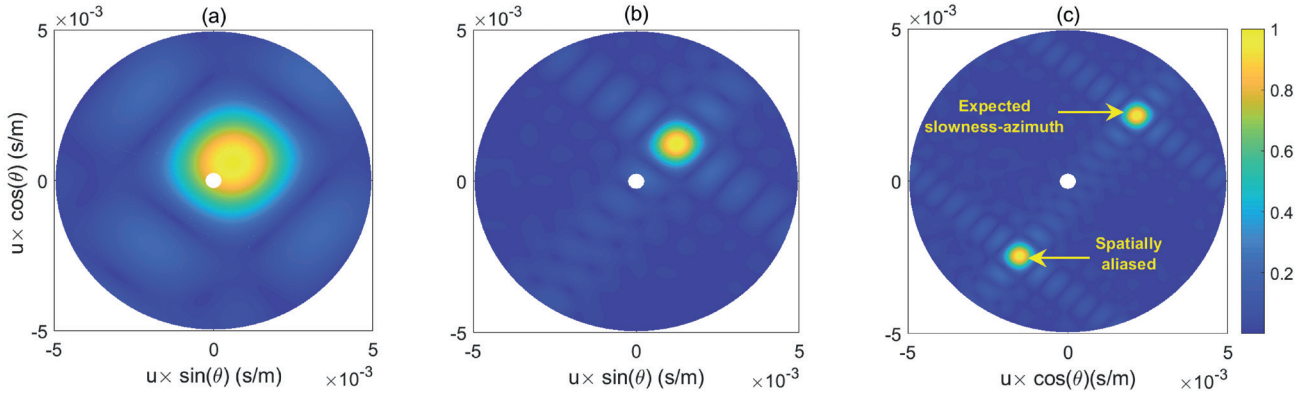

Figure 2 Theoretical array response values (shown using the colourbar) for a plane wave impinging the array of seismic sensors shown in Figure 1a corresponding to (a) velocity of 1200 m/s, propagation azimuth of 45° at a frequency of 0.4 Hz, (b) velocity of 570 m/s, propagation azimuth of 45° at a frequency of 1.0 Hz, and (c) velocity of 330 m/s, propagation azimuth of 45° at a frequency of 1.7 Hz.

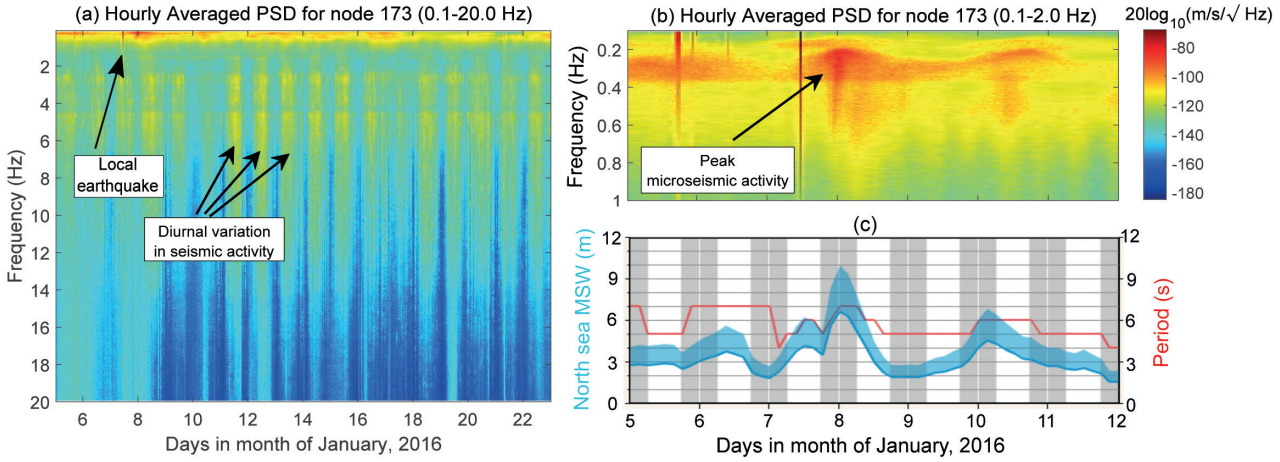

Figure 3 a) Spectrogram of the seismic ground velocity measured by Sensor 173 for the entire measurement period between 5-22 January, 2016 with a temporal resolution of one hour and in the frequency band 0.1 to 20 Hz. Typical diurnal variations due to man-made seismic noise is observed. An earthquake of moment magnitude 1.7 with its epicentre at Zuidbroeke measured on 7 January, 2016 is also shown. b) Zoomed spectrogram in the frequency band 0.1 to 1.0 Hz showing the temporal variation of the secondary microseism energy. c) Observed MSW of the North Sea (blue curve) between 5 and 11 January, 2016 and the dominant wave period (red curve) measured during the same time.

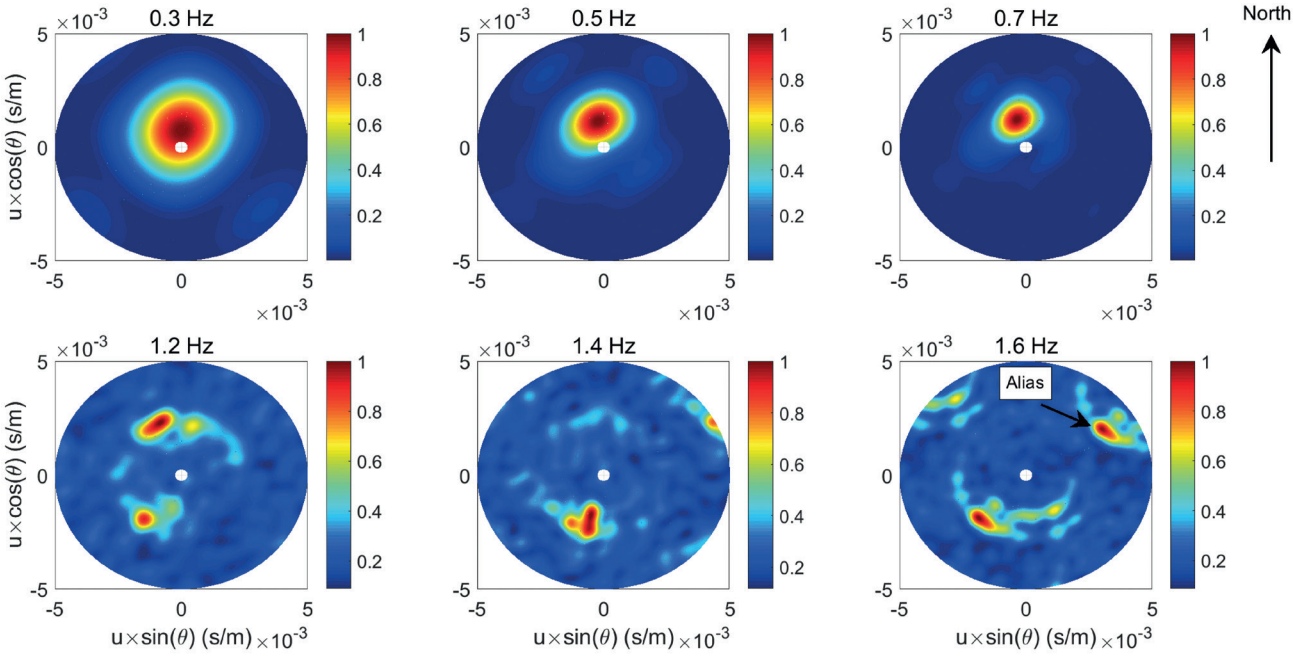

Figure 4 Beamforming output for 8 January, 2016 with slowness 2.5 × 10^{-4} to 5 × 10^{-3} s/m on the radial axis and azimuth in the range 0 to 359.5° at frequencies of 0.3, 0.5, 0.7, 1.2, 1.4 and 1.6 Hz.

correlated to the observed mean significant wave height (MSW) in the North Sea during that day as shown in Figure 3c. A trough in the ground motion spectrum is observed between 0.7 and 1 Hz which agrees very well with global observations (Peterson et al., 1993). The frequency band 1.5 ~~and~~ 5 Hz is mostly dominated by ground motion generated by human activities and regional earthquakes of shallow origin. Two peaks, one centered at 3 Hz and the other at 5 Hz are observed during all days of measurement which corresponds to noise from a road running South-West of the seismic array. The noise level in this band varies within half an order of magnitude over all days of measurement. Since the high-frequency noise is dominantly man-made, PSDs estimated during the day are higher than that measured at night by an order of magnitude. At frequencies greater than 5 Hz, the noise sources are mostly local and transient. This is also the reason that the diurnal variation of the measured PSD level spans over two orders of magnitude, an order of magnitude higher than that observed for frequencies below 5 Hz.

Beamforming results

This method first proposed by Lacoss et al. (1969) makes use of the beampower to estimate the steering vector that most closely resembles the actual direction of propagation θ and slowness u of the seismic noise. The beampower $BP(f)$ at frequency f and corresponding to a steering vector $a_k(f)$ is evaluated as,

$$BP(f) = a_k^*(f) R_{xx}(f) a_k(f) \quad (1)$$

$R_{xx}(f)$ is the data covariance matrix in frequency domain, and $a_k^*(f)$ represents the complex conjugate of the steering vector corresponding to the k^{th} combination of u, θ. The combination of u, θ corresponding to the maximum value of beampower, gives an estimate of the propagation direction and slowness at frequency f. Beamforming was performed at first on every hour of data with each hour of data being subdivided into ~~ten~~ minute windows and an overlap of 50% between consecutive windows. The beampower for every hour of data was computed following Equation 1. Trial array response vectors were used in the slowness range 2.5×10^{-4} to 5×10^{-3} s/m at an interval of 8.33×10^{-6} s/m, and in the azimuth range 0 to 359.5° at an interval of 0.5°. Beampowers computed hourly as a function of slowness and azimuth are then averaged for all hours of the day. As was the case for Figure 2 we plot the beampower as a function of slowness (u) and azimuth (θ) on a polar graph, where the slowness increases radially outwards and the azimuth is measured clockwise from the North. Figure 4 shows the beampower plotted as a function of slowness-azimuth at frequencies of 0.3, 0.5, 0.7, 1.2, 1.4 and ~~1.7~~ Hz. In the frequency band 0.2 to 1.2 Hz, beamforming shows the dominant noise direction to be northwest which explains their oceanic origin (Spica et al., 2018). At frequencies above 1.2 Hz, noise originating south of the array appears as a semi-circular arc. This corresponds to the noise due to a nearby road that borders the Southern edge of the array. At 1.6 Hz, an alias of the noise source is observed and is marked in Figure 4. The true azimuth and velocity of propagation of the surface waves at 1.6 Hz are 227° (measured clockwise from north) and 384 m/s respectively. The alias is observed at an azimuth of 32° and a velocity of 227 m/s. An easy way of removing such an aliased surface wave arrival is to interpret the observations using the theoretical array response estimates (for this case, if we limit the minimum velocity to 300 m/s instead of 200 m/s which is the value used for computing the beampowers as shown in Figure 4, we can remove the alias from the new $u - \theta$ domain). However, at high frequencies with the presence of many such aliases in $u - \theta$ domain, it is practically impossible to select a specific slowness range without any prior idea of the expected dispersion of the surface waves. Hence, extraction of the dispersion curve for this array was limited to a maximum of 1.7 Hz.

Extended spectral auto-correlation

The ESAC method was first introduced by Ling and Okada (1993), following the work of Aki (1957). Since it is based on the Spectral Auto-correlation (SAC) method, we first discuss the SAC method briefly before describing the ESAC method. The normalized cross-spectra of the seismic data between the m^{th} and n^{th} sensors can be expressed as

$$S_{mn}(f) = \frac{\frac{1}{M}\sum_{i=1}^{M} S_{mn}^{i}(f)}{\sqrt{\frac{1}{M^2}\sum_{i=1}^{M} S_{mm}^{i}(f)\sum_{i=1}^{M} S_{nn}^{i}(f)}} \quad (2)$$

where f represents the frequency, S_{mn}^{i} the cross-spectrum for the i^{th} data segment, and M the total number of data segments. We consider an array layout with N seismic sensors, such that we have one sensor at the centre which coincides with some chosen origin and the remaining sensors are distributed equally spaced in azimuth along the circumference of a circle. In practice, sensors are distributed along the circumference of several such circles of increasing radii. Then the cross-spectrum between the m^{th} sensor with location coordinate (x_m, y_m) and the n^{th} sensor with location coordinate x_n, y_n can be rewritten in the form $S_{mm}(f, r_{mn})$, where $r_{mn} = \left\{(x_m - x_n)^2 + (y_m - y_n)^2\right\}^{1/2}$. Considering $m = 0$, which corresponds to the sensor at the center of the array and $r_{0n} = r$, we can then write the azimuthally averaged cross-correlation function as

$$S(f,r) = \frac{1}{N-1}\sum_{n=1}^{N-1} \Re\left(S_{0n}(f,r)\right) \quad (3)$$

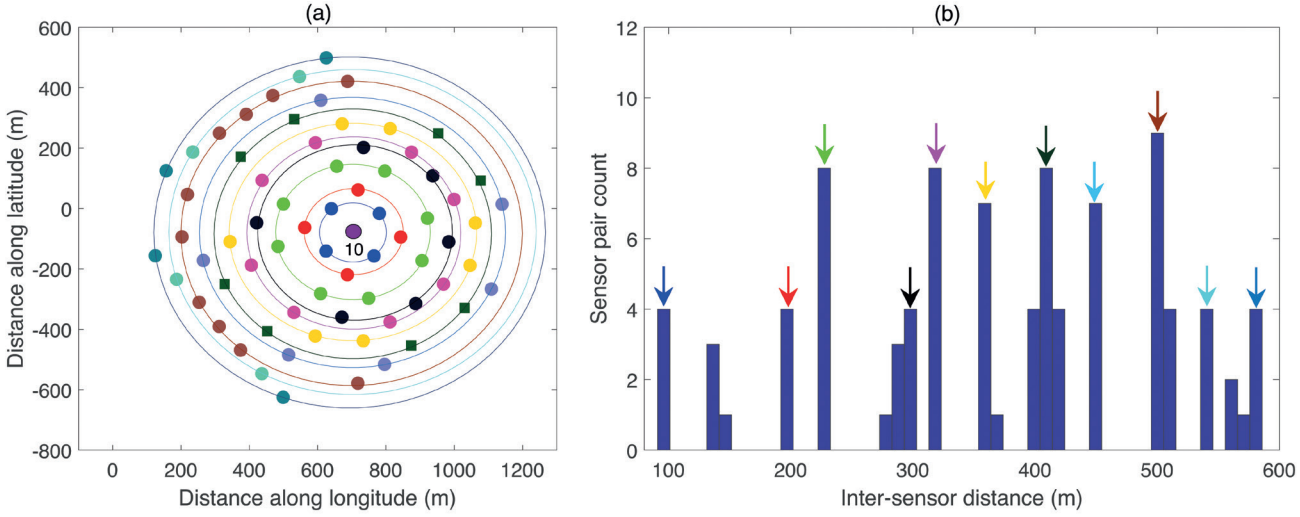

Figure 5 a) Layout of the sensors used for the SAC method with sensor locations that lie on a circle of fixed radius (error: ±10 m) shown with a distinct colour and the central sensor marked as 10. b) Histogram of the distances of the all the sensors from the central sensor with a distance bin size of 10 m and the arrows with different colours point to each collection of sensors that lie on a circle of fixed radius (shown in a).

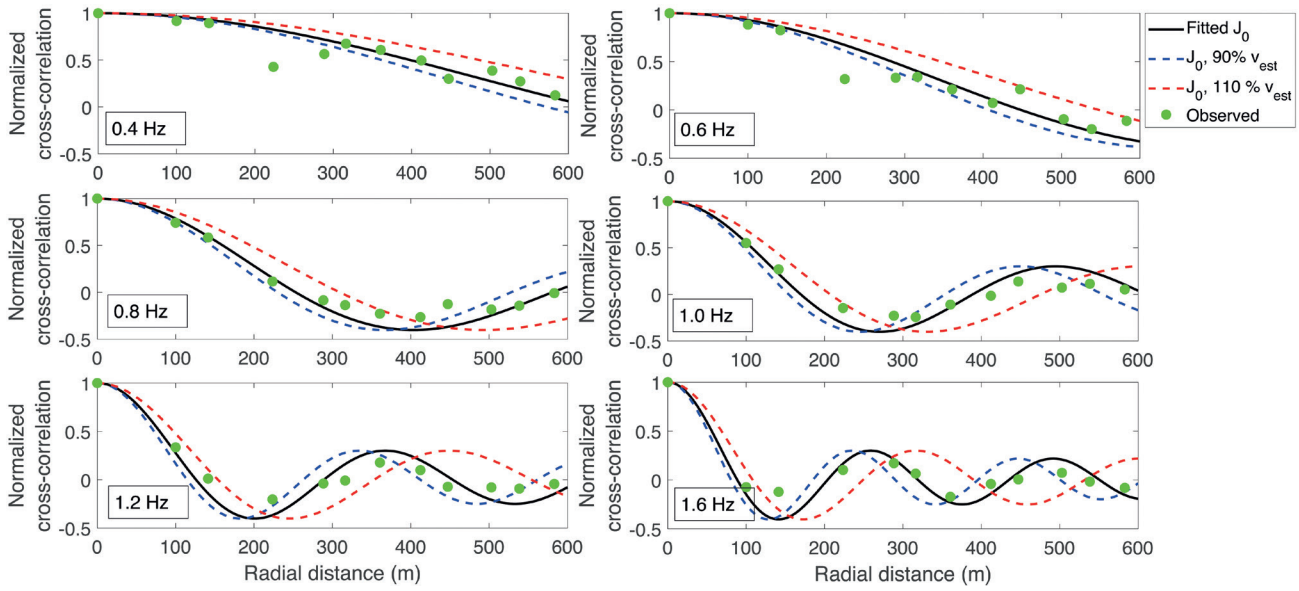

Figure 6 Spatially averaged real value of the normalized cross-correlation expressed as function of the radius of the rings shown with the green dots and the best fitting zeroth order Bessel function shown by the black curve at frequencies of 0.4, 0.6, 0.8, 1.0, 1.2 and 1.6 Hz. The dotted red and blue curves show the Bessel functions corresponding to ±10% error in the estimated phase velocity.

Following the work of Aki (1957) the phase velocity $c(f)$ of the propagating surface wave between a receiver pair in a homogeneous random field can be obtained from

$$S(f,r) = J_0\left(\frac{2\pi fr}{c(f)}\right) \tag{4}$$

Where J_0 is the zero-th order Bessel function. In order to estimate the phase velocity from Equation 4 we must either keep the radius r constant and vary f or vice versa. Since the phase velocity is a function of frequency, keeping the frequency constant and then trying to satisfy Equation 4 is deemed suitable. The azimuthal averaging of the cross-spectrum data performed in Equation 3 needs the sensors to be spaced equally in azimuth along the circumference of the circle of radius r, and it is one of the limitations of the SAC method. However, the ESAC method remedies this constraint in the array design by using a slightly modified version of Equation 4. The phase velocity $c(f)$ is found to satisfy the following equation in a least square sense,

$$S_{0n}(f,r_{0n}) = J_0\left(\frac{2\pi fr_{0n}}{c(f)}\right) \tag{5}$$

where $n = \{1,2,3,\ldots N-1\}$ are the number of sensors surrounding one central sensor positioned at the origin of the array layout. The phase velocity $c(f)$ is estimated by fixing the frequency at a particular value and then fitting the zero-th order Bessel function, which is now only a function of the radial distance r_{0n} The best fitting Bessel function is obtained by minimizing the error function

$$E(f) = \sum_{n=1}^{N-1}\left(S_{0n}(f,r_{0n}) - J_0\left(\frac{2\pi fr_{0n}}{c(f)}\right)\right) \tag{6}$$

The array of 96 sensors deployed in Groningen extends up to a maximum of 1000 m along two orthogonal directions. Hence, we select sensor number 10 approximately located in the center of the array and as shown in Figure 5a as the central sensor. This is followed by binning the distance of each sensor in the array from the selected central sensor. A histogram of these inter-sensor distances is computed for a bin size of 10 m, and then the distance bins that comprise greater than four sensors are selected for the analysis. A total of 11 such distance bins are identified and their respective distances from the central sensor are shown with arrows marked in the histogram plot in Figure 5b. For clarity, the circles corresponding to each of these selected distance bins are also shown in Figure 5a with the sensors and the respective circle passing through the group of sensors plotted with a distinct colour. The radius of each circle is computed as the mean of the distance of the sensors in that group from the central sensor. Now, since the sensors are partitioned into groups with a bin size of 10 m, all the sensors classified to a particular circle might not exactly lie on the circumference. We also note that for inter-sensor distances above 500 m, the azimuthal coverage of the sensor positions in the last three rings is skewed.

After the selection of the central sensor and classifying the sensor locations into different circles, we now select the data window length and the percentage of overlap for computing the cross-spectrum following Equation 2. We select a window length of 10 minutes and an overlap of 50% between consecutive windows. First we compute the cross-spectrum between the central sensor and all the sensors that belong to one particular ring as shown in Figure 5a. The temporal averaging of the cross-spectrum between the central sensor and another sensor on a given circle is carried out for a day of seismic data. After the temporal averaging of the cross-spectrum has been done, we perform a spatial averaging by using the temporally averaged cross-spectrum from all the sensors that were ~~classified to~~ a particular ring. The spatially averaged cross-spectra which are just a function of frequency are then assigned to the circle in consideration. This process is then repeated for all the rings, such that at each frequency we have cross-spectrum magnitudes as a function of radius of the rings.

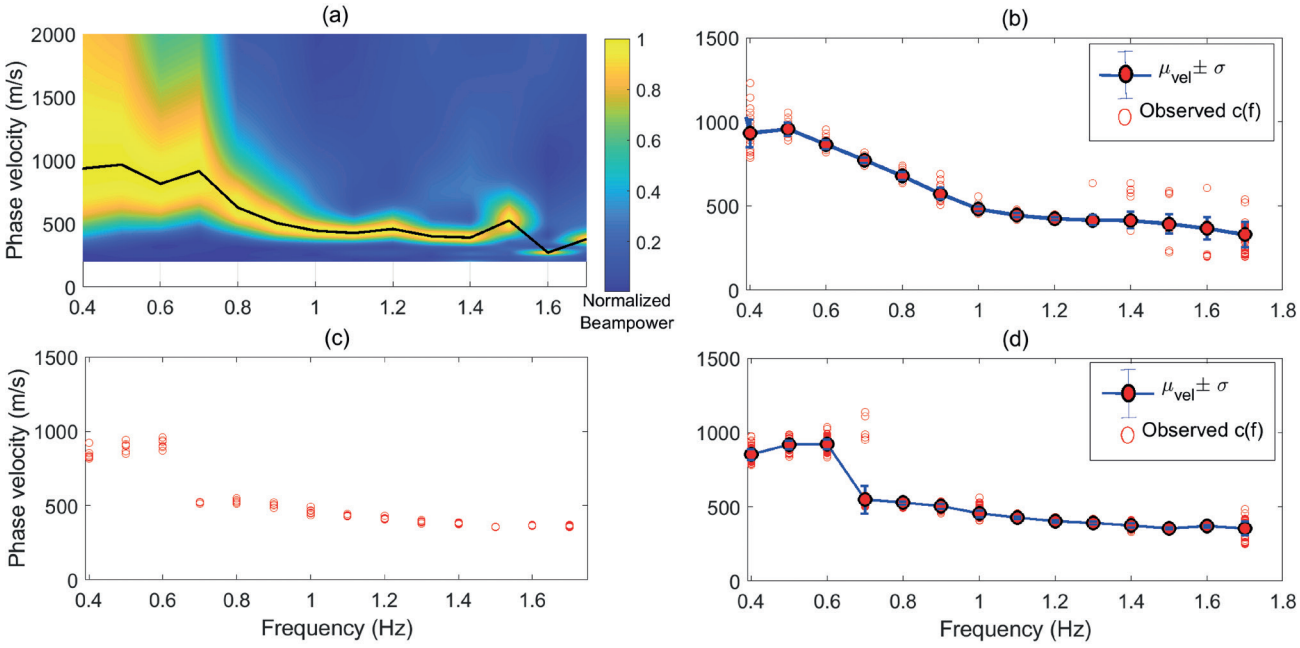

Figure 7 a) Azimuthally averaged beampower computed for a day of ambient noise recording on 12 January, 2016 plotted as a function of velocity and frequency, with the black curve showing the observed Rayleigh wave dispersion. b) Observed (red dots) and mean Rayleigh wave phase velocity (solid blue curve) with the respective standard deviations (blue vertical lines) obtained from beamforming analysis of ambient noise recorded between 5 and 22 January, 2016 at an interval of 0.1 Hz in the frequency band 0.4 to 1.7 Hz. c) Estimated Rayleigh wave phase velocity (red dots) plotted as a function of frequency obtained from ESAC analysis of every hour of ambient noise data recorded on 12 January, 2016. d) Observed (red dots) and mean Rayleigh wave phase velocity (solid blue curve) with the respective standard deviations (blue vertical lines) obtained from ESAC analysis of ambient noise recorded between 5 and 22 January, 2016 at an interval of 0.1 Hz in the frequency band 0.4 to 1.7 Hz.

Figure 6 shows the cross-spectrum magnitudes obtained using Equation 3 as a function of radius at six different frequencies of 0.4, 0.6, 0.8, 1.0, 1.2 and 1.6 Hz. The black curve which corresponds to the best fitting zeroth order Bessel function, as expressed in Equation 4, is fitted to the observed cross-correlations by minimizing the error function in Equation 5 by applying the Marquadt least-square method. Repeating this minimization scheme at the desired set of frequencies gives us the phase velocity $c(f)$ as a function of frequency. In Figure 6 we also plot the Bessel functions corresponding to a 10% error in the estimated phase velocity. Most of the observed cross-correlation magnitudes shown as the green dots in Figure 6 lie within the blue and the red dotted curves corresponding to ±10% error in the estimated phase velocity respectively.

Rayleigh wave phase velocity

Up to this point we have discussed the two methodologies that can be used for estimating the phase velocity and the direction of propagation of Rayleigh waves. The ESAC method directly gives us an estimate of the phase velocity $c(f)$ upon solving the minimization problem stated in Equation 6. In order to obtain the phase velocity as a function of frequency, we need to express the beampower only as a function of u and f. We sum the beampower across all values of azimuth for a particular slowness and frequency. Following this, we pick the slowness value corresponding to the maximum beampower. Repeating this process over all frequencies yields the Rayleigh wave dispersion.

Figure 7a corresponds to the average beampower for a day of seismic noise recording. The black curve in Figure 7a joins the slowness values corresponding to the maximum beampower at each frequency. Figure 7b shows a scatter plot of the estimated dispersion curves obtained from beamforming analysis of all 18 days of ambient noise recordings. The mean dispersion curve is shown with the blue solid curve and the associated standard deviation of the observed phase velocity at each frequency shown with the error bars. Due to the limited maximum aperture of the array, we observe that the error associated with the phase velocity estimation at frequencies below 0.6 Hz is considerably higher as compared to the high frequencies. Figure 7c shows a scatter plot of the phase velocities as a function of frequency obtained from ESAC analysis of a day of ambient noise recordings. Figure 7d shows the scatter of the observed phase velocity dispersion obtained from the ESAC analysis of all 18 days of ambient noise recording. The solid blue line shows the mean phase velocity from all the observations and the standard deviation is shown using the error bars.

Conclusion

Comparing the mean phase velocities obtained from beamforming and ESAC analysis, a good agreement is observed for frequencies greater than 0.8 Hz. In the frequency band 0.4 to 0.8 Hz the phase velocities obtained from ESAC show a few jumps especially between 0.6 and 0.7 Hz. This artefact observed in the ESAC results can be ascribed to two factors. Firstly, the noise source in the frequency band is microseismic in origin and has a fixed azimuth of 330° measured clockwise from the north, and the very assumption that long period ambient noise recordings tend to depict an isotropic noise source distribution does not hold. Secondly, due to inadequate azimuthal coverage of the sensors in the rings with higher inter-sensor separation (greater than 500 m), the spatial averaging of cross-correlation magnitudes inherent with the SAC method does not overcome the directional bias in

the observations. The fundamental difference between the SAC method and the ESAC method is in the way the cross-spectrum of the seismic data is used. While the SAC method uses an azimuthal averaging of the computed cross-spectrum between one central sensor and the sensors placed on the circumference of a circle, the ESAC method relies on simply using the temporally averaged cross-spectrum between a central sensor and the rest of the sensors, irrespective of their position in the array layout. In reality, the temporal averaging of the cross-spectrum of the seismic data over long time periods is a substitute to positioning the sensors on a circumference of a circle. Over long periods of ambient noise recording, the assumption that noise sources originate from all directions and can be treated as a stationary random field is the key behind the working of the ESAC method. In other words, the azimuthal averaging performed in the SAC method by positioning sensors at equally spaced azimuth and at a fixed radial distance from the central sensor is equivalent to using just one sensor pair and instead positioning the noise sources equally spaced in azimuth on a circle around the sensor pair. As a result, the SAC method always works even if the noise source distribution around the array layout is not azimuthally isotropic. It is also the reason why the ESAC method might not work if the temporal averaging of the cross-spectrum is over short time spans and the noise source distribution around the sensor pair is not isotropic. From the passive study at Groningen we observe that at higher frequencies the noise source distribution tends to be well distributed in azimuth and hence the phase velocity estimates from beamforming and ESAC are close.

References

Aki, K. [1957]. Space and time spectra of stationary stochastic waves, with special reference to microtremors. *Bull. Earthq. Res. Inst*., **35**, 415–456.

Asten, M. and Henstridge, J. [1984]. Array estimators and the use of microseisms for reconnaissance of sedimentary basins. *Geophysics*, **49** (11), 1828–1837.

Beker, M., Campman, X., Oven, van J., Walk, W., Levell, J., Tang, Z., Danilouchkine, M., Smit, D., Brand, J.v.d., Koley, S. and Bader M. [2017]. Innovations in seismic sensors driven by the search for gravitational waves. *The Leading Edge*, **35** (7), 590–593.

Chouet, B., De Luca, G., Milana, G., Dawson, P., Martini, M. and Scarpa, R. [1998]. Shallow velocity structure of Stromboli volcano, Italy, derived from small-aperture array measurements of Strombolian tremor. *Bulletin of the Seismological Society of America*, **88** (3), 653–666.

Draganov, D., Campman, X., Thorbecke J., Verdel, A. and Wapenaar, K. [2009]. Reflection images from ambient seismic noise. *Geophysics*, **74** (5), A63–A67.

Horike, M. [1985]. Inversion of phase velocity of long-period microtremors to the S-wave velocity structure down to the basement in urbanized areas," *Journal of Physics of the Earth*, **33** (2), 59–96.

Kimman, W. and Trampert, J. [2010]. Approximations in seismic interferometry and their effects on surface waves. *Geophysical Journal International*, **182** (1), 461–476.

Kimman, W., Campman, X. and Trampert, J. [2012]. Characteristics of seismic noise: fundamental and higher mode energy observed in the Northeast of the Netherlands, *Bulletin of the Seismological Society of America*, **102** (4), 1388–1399.

Koley, S., Bulten, H.J., Brand, J.v.D., Bader, M., Campman, X. and Beker, M. [2017]. S-wave velocity model estimation using ambient seismic noise at Virgo, Italy. *SEG Technical Program Expanded Abstracts*, 2946–2950.

Lacoss, R.T., Kelly, E.J. and Toksöz, M.N. [1969]. Estimation of seismic noise structure using arrays. *Geophysics*, **34** (1), 21–38, 1969.

Ling, S. and Okada, H. [1993]. An extended use of spatial autocorrelation method for the estimation of structure using microtremors. *89th SEGJ Conference*, 44–48.

Marquadt, D. [1963]. An algorithm for least square minimization of nonlinear parameters. *SIAM Journal*, **11**.

Ohori, M., Nobata, A. and Wakamatsu, K. [2002]. A comparison of ESAC and FK methods of estimating phase velocity using arbitrarily shaped microtremor arrays. *Bulletin of the Seismological Society of America*, **92** (6), 2323–2332.

Okada, H. [1987]. Comparison of spatial autocorrelation method and frequency-wavenumber spectral method of estimating the phase velocity of Rayleigh waves in long-period microtremors. *Geophysical Bulletin of Hokkaido University*, **49**, 53–62.

Park, C.B., Miller, R. D. and Xia, J. [1999]. Multichannel analysis of surface waves. *Geophysics*, **64** (3), 800–808.

Peterson, J. [1993]. *Observations and modeling of seismic background noise*. Open-File Report, 93-322.

Spica, Z.J., Nakata, N., Liu, X., Campman, X., Tang, Z. and Beroza G.C. [2018]. The Ambient Seismic Field at Groningen Gas Field: An Overview from the Surface to Reservoir Depth. *Seismological Research Letters*, **89** (4), 1450–1466.

Woods, J.W. and Lintz, P.R. [1973]. Plane waves at small arrays. *Geophysics*, **38**, 1023–1041.